Seasonal Cycle of Cross-Equatorial Flow in the Central Indian Ocean

Yi Wang[1], Michael J. McPhaden[2]

[1]Physical Oceanography Laboratory, Ocean University of China, Qingdao, China

[2]Pacific Marine Environmental Laboratory, National Oceanic and Atmospheric Administration, Seattle, WA, USA

Corresponding author: Yi Wang (Emmet.yi.wang@gmail.com)

Key Points

- Mean volume transport is southwards across the equator in the central Indian Ocean in approximate Sverdrup balance with the wind stress curl
- Meridional winds force a northward flow near the surface above deeper southward flow to generate an equatorial roll in the surface layer
- Surface layer Ekman convergence and thermocline geostrophic divergence is superimposed on annual variations in cross equatorial flow

Abstract

This study investigates the seasonal cycle of meridional currents in the upper layers of central equatorial Indian Ocean using acoustic Doppler current profiler (ADCP) and other data over the period 2004-2013. The ADCP data set collected along 80.5°E is the most comprehensive collection of direct velocity measurements in the central Indian Ocean to date, providing new insights into the meridional circulation in this region. We find that mean volume transport is southwards across the equator in the central Indian Ocean in approximate Sverdrup balance with the wind stress curl. In addition, mean westerly wind stress near the equator drives convergent Ekman flow in the surface layer and subsurface divergent geostrophic flow in the thermocline at 50-150 m depths. In response to a mean northward component of the surface wind stress, the maximum surface layer convergence is shifted off the equator to 0.75°N. Evidence is also presented for the existence of a shallow equatorial roll consisting of a northward wind-driven surface drift overlaying the southward-directed subsurface Sverdrup transport. Seasonal variations are characterized by cross equatorial transports flowing from the summer to the winter hemisphere in quasi-steady Sverdrup balance with the wind stress curl. In addition, semi-annually varying westerly monsoon transition winds lead to semi-annual enhancements of surface layer Ekman convergence and geostrophic divergence in the thermocline. These results quantify expectations from ocean circulation theories for equatorial Indian Ocean meridional circulation patterns with a high degree of confidence given the length of the data records.

1. Introduction

Unlike the equatorial Pacific and Atlantic Oceans where relatively steady easterly trade winds prevail, the equatorial Indian Ocean is dominated by seasonally reversing monsoon winds [*Schott and McCreary,* 2001*; Schott et al.,* 2009]. Along the equator, winds are westerly during the transitions between the northeast and southwest monsoons and, in the mean, are also westerly rather than easterly as in the other two ocean basins. In addition, the seasonally varying zonal wind stress is nearly anti-symmetric around the equator, with a structure that favors southward cross equatorial transport in the upper layer of the ocean during the boreal summer monsoon and northward transport during the winter monsoon (Figure 1a and 1b) [*Schott et al.,* 2002*; Miyama et al.,* 2003*; Schott et al.,* 2004*; Schott et al.,* 2009*; Horii et al.,* 2013]. Southward transports in boreal summer connect the upwelling zones in the Northern Hemisphere (primarily off Somalia) and the subduction zone in the southeastern Indian Ocean, forming a cross-equatorial meridional overturning cell [*Wacongne and Pacanowski,* 1996*; Garternicht and Schott,* 1997*; Lee and Marotzke,* 1997*;* 1998*; Schott and McCreary,* 2001*; Miyama et al.,* 2003]. During the boreal winter monsoon, the circulation reverses direction. Hence, the meridional currents and their seasonal cycle at the equatorial region play a key role in the interhemispheric exchange of mass and heat in the Indian Ocean [*Hsiung,* 1985*; Hsiung et al.,* 1987*; Wacongne and Pacanowski,* 1996*; Chirokova and Webster,* 2006*;*].

Most studies of the near equatorial circulation in the Indian Ocean have focused on the zonal flows of the Wyrtki jets for which the signal is very large [*Wyrtki,* 1973; *McPhaden, 1982; Hastenrath and Greischar,* 1991]. On the other hand, previous studies of the meridional circulation have been hampered by relatively weak seasonal signals in meridional vis-à-vis zonal velocity combined with a paucity of direct velocity observations. Variations in meridional currents in the equatorial Indian Ocean have therefore been studied primarily via numerical modeling simulations guided by a limited amount of observational data [*Jensen,* 1993*; McCreary et al.,* 1993*; Lee and Marotzke,* 1997*; Miyama et al.,* 2003*; Schott et al.,* 2002*; Schott et al.,* 2004*; Chirokova and Webster,* 2006*; Pérez-Hernández et al.,* 2012*; Rao et al.,* 2016]. For example, Schott et al. [2002] analyzed moored acoustic Doppler current profiler (ADCP) time series centered at 0°, 80.5°E from the World Ocean Circulation Experiment (WOCE) during 1993-1994 [*Reppin et al.,* 1999] and inferred that near surface cross equatorial meridional currents were governed by Ekman dynamics, consistent with theoretical considerations and model simulations [*e.g. Miyama et al.,* 2003]. However, data used in the *Schott et al.* study covered only 15 months during an El Niño event and one of the strongest Indian Ocean Dipole (IOD) events of 20th century. Thus, representativeness of their results for longer periods is open to question. Also, due to the lack of data, their interpretation of the meridional circulation in terms of Miyama's [2003] theory for cross-equatorial flow did not focus on equatorial wave dynamics and associated zonal pressure gradients, which are significant along the equator [*Nagura and McPhaden,* 2008*,* 2010a,b]. Horii et al. [2013] analyzed ADCP data from moorings at 0°, 80.5°E and 0°, 90°E for November 2004 to August 2008 and January 2001 to December 2008, respectively and also found that annual mean meridional currents were dominated by the boreal summer monsoon during which meridional transports were southward across the equator. However, the strength and phase of the observed meridional transports and the theoretically estimated Sverdrup and Ekman transports based on *Miyama et al.* [2003] did not agree well in their study. Horii et al. [2013] attributed the discrepancy between observations and theory to the presence of significant zonal wind stress forcing in the central equatorial Indian Ocean, as suggested in *Schott et al.* [2002].

Here we expand on these studies to describe the meridional structure of the mean seasonal cycle in upper ocean meridional currents near the equator and then to investigate their dynamics. We use nine years (November 2004 to October 2013) of velocity data from a mooring site 0°, 80.5°E and five years (August 2008 to August 2013) of velocity data at seven additional sites along 80.5°E between 4°S and 2.5°N (Figure 1). These unique data come from an array of upward-looking ADCPs mounted on subsurface moorings embedded within the Research Moored Array for Africa Asian Australian Monsoon Analysis and Prediction (RAMA) program [*McPhaden et al.,* 2009]. The 80.5°E meridian is in a region where previous observational and modeling studies suggest that wind driven current variations exhibit a robust seasonal cycle. In contrast to earlier observational work that relied on data of either limited duration [*e.g., Reppin et al.,* 1999*; Schott et al.,* 2002] or latitudinal extent [e.g., *Horii et al.,* 2013; *Rao et al.,* 2016], here we are able to examine in much greater detail the meridional and vertical structure of the meridional flow field in the central equatorial Indian Ocean. Our multi-year time series also provide great discriminating power in testing hypotheses about how the flow in this region responds to that wind forcing.

2. Data Description

The horizontal velocity data used in this study were collected from subsurface ADCP moorings at 8 sites along 80.5°E: 4°S, 2.5°S, 1.5°S, 0.75°S, 0°, 0.75°N, 1.5°N, and 2.5°N

(Figure 1). The ADCPs were mounted in floats located at depths of about 300-400 m. The data span November 2004 to October 2013 at 0°and August 2008 to August 2013 at other sites (Figure 1c). Daily averaged velocity data were gridded to uniform 5 m bin widths after adjusting depths based on speed of sound information from historical CTD's near the mooring.

Due to reflection of acoustic signals from the air-sea interface, we removed data shallower than 35 m and extrapolated velocity to the surface using a quadratic spline extrapolation. We evaluated the extrapolated values by comparing with point Sontek acoustic Doppler current meter records at 10 m depth from the 1.5°S, 0°, 1.5°N moorings along 80.5°E (Figure 1c). As a measure of success for this procedure, the correlation coefficient between extrapolated and measured time series reaches 0.80 with a regression slope close to unity (Figure 2a). The root mean square difference between the measured data and extrapolated data (0.10 m s^{-1}) is likewise smaller than the standard deviation of the measure data (0.14 m s^{-1}).

Data gaps in the time series were filled via linear least squares orthogonal regression based on velocities at adjacent sites. To test the accuracy of this procedure, meridional velocities during one deployment from May 2010 to July 2011 at 0.75°N, 80.5°E were removed and then filled via regression. Correlation between the filled and actual velocities is high (coefficient of 0.87) and significant, with a regression slope close to unity (Figure 2b). The root mean square deviation between the actual data and filled data (0.07 m s^{-1}) is significantly smaller than the standard deviation of the actual velocities (0.13 m s^{-1}). These results give us confidence that our gap filling procedures are sufficiently accurate to produce continuous time series for further analysis.

An example of a time series filled using these methods at 0°, 80.5°E (Figure 3) shows the predominance of energetic biweekly waves near the equator [*Sengupta et al.,* 2004]. The presence of these energetic waves means that multi-year records, like we have collected, are needed to compute reliable estimates of the mean and mean seasonal cycle of meridional velocity in this region. More details on data characteristics and quality control can be found in *Wang et al.* [2015] and *McPhaden et al.* [2015].

For estimates of wind stress, we use daily mean Tropflux data, which are available on a 1° latitude by 1° longitude grid [*Praveen Kumar et al.,* 2013]. Tropflux stresses are based on the COARE v3.0 algorithm using a bias and amplitude corrected ERA-I reanalysis product as input. In a comparison with other widely used daily wind stress products (NCEP, NCEP2, ERA-I and QuikSCAT), Tropflux performs best in the equatorial oceans [*Kumar et al.,* 2013]. To interpret the 5- and 9-year long velocity records, we computed the mean seasonal cycle of the wind stress by averaging the data from each day and month across years for the period August 2008 to August 2013 (a 5-year climatology) and November 2004 to October 2013 (a 9-year climatology). To check the representativeness of these climatologies based on five to nine years of data, we also calculated a climatology based on 34 years of data, from January 1979 to December 2013.

We are interested in separating Ekman and geostrophic velocity contribution to the total velocity. Therefore, we compute zonal pressure gradients using absolute dynamic height (ADH) data, which are derived from the Argo plus Aviso altimetry (http://apdrc.soest.hawaii.edu/projects/Argo/data/Documentation/gridded-var.pdf) on a 1° x 1°

latitude/longitude grid by the International Pacific Research Center (IPRC). The ADH is defined as the sea surface height (SSH) minus the geopotential height from the surface to a certain level. The seasonal cycle of zonal pressure gradients is computed using 10° centered differences around 80.5°E (i.e. 80.5°E ± 5°) of monthly ADH data for the same period as the wind stress data (namely, August 2008 to August 2013). Calculations of this pressure gradient are relatively insensitive to using centered differences over intervals from 4° to 16° of longitude. For the ± 5° span of longitudes over which we calculate these zonal pressure gradients, there are 3461 Argo profiles from 79 floats distributed between August 2008 and August 2013. Thus, we expect that these gradient estimates are well constrained by the observations.

To characterize the uncertainties in our seasonal cycle estimates, we compute standard errors ($\sigma_{\bar{x}}$) using the conventional formula $\sigma_{\bar{x}} = \sigma/\sqrt{n}$ Where σ is the standard deviation and n is the number of degrees of freedom. For n, we choose the number of full years in the time series, assuming each year is independent (e.g., 9 degrees of freedom for the means in Figure 3b). Error estimates for ± one standard error are presented in Figures 3-5 and 7.

3. Results

3.1 Mean Meridional Structure

Mean winds near the equator in the Indian Ocean are dominated by the strong southwesterly monsoons. Thus, wind stress near the equator has a westerly component on average (Figure 4a), which is stronger to the north than to the south, and a southerly component to the meridional wind stress. From the sign of the zonal winds one would therefore expect Ekman convergence near the surface and geostrophic divergence in the thermocline in contrast to what is observed in the equatorial Pacific and Atlantic where easterly trade winds prevail [*Johnson et al.,* 2001; *Rabe et al.,* 2008]. This circulation indeed emerges from the 5-year average of the moored meridional currents (Figure 4b). In particular, there is a marked divergence between about 50-150 m in the thermocline, with a weaker convergence near the surface. The divergence is consistent with the poleward geostrophic currents in each hemisphere driven by negative pressure gradient force in balance with the westerly wind stress (see also *Nagura and McPhaden*, 2008). The surface layer convergence is shifted upwind off the equator to about 1°N while divergence is evident to the south of the equator in response to the mean southerly winds, features that are consistent with near equatorial surface layer Ekman dynamics in the response to meridional wind forcing [*Cromwell,* 1953*; De Szoeke et al.,* 2007].

The sign of the mean wind stress curl, which is largely determined by the zonal component of wind stress near the equator in the Indian Ocean, is mostly negative between 4°S and 2.5°N (Figure 4a). This curl would be expected to drive mean southward volume transports on both sides of the equator in the upper ocean in approximate Sverdrup balance, namely $V_{Sv}=(\rho\beta)^{-1}\mathrm{Curl}\ \boldsymbol{\tau}$, where V is meridional transport, ρ is mean density, β is the meridional gradient of the Coriolis parameter f on the equatorial beta plane (i.e., $f=\beta y$) and τ is vector wind stress [*Horii et al.,* 2013*; Miyama et al.,* 2003*; Reppin et al.,* 1999*; Schott and McCreary,* 2001*; Schott et al.,* 2002*; Schott et al.,* 2004*; Schott et al.,* 2009]. The mean meridional current profiles are predominantly southward in the upper 150 m south of 1.5°N, consistent with this expectation. However, it is noteworthy that at and north of 1.5°N, subsurface northward flow is both stronger and vertically broader than the near surface southward current. This is related to the fact that both mean zonal winds and wind stress curl evolve meridionally, with the wind stress curl trending towards zero and the mean zonal winds strengthening from south to north. Thus, assuming Sverdrup dynamics applies, southward Sverdrup transport should weaken towards the north while at the same time northward geostrophic flow in the thermocline, in balance with the zonal pressure gradient set up by the westerly winds, should become more prominent.

As noted earlier, the meridional component of the wind stress is weak but northward at all latitudes (Figure 4a), which drives the shallow northward flow near the equator where Coriolis force is negligible. Within 0.75° of the equator, this northward flow overlays the net southward Sverdrup transport driven by the negative wind stress curl (Figure 3b and 4b). This near-surface equatorial overturning cell is referred to as the equatorial roll [*Wacongne and Pacanowski,* 1996*; Miyama et al.,* 2003*; Schott et al.,* 2002*; Schott et al.,* 2004*; Schott et al.,* 2009]. Our analysis provides observational confirmation of this unique Indian Ocean circulation feature, which is narrowly confined to the equatorial band (±0.75°) and depths shallower than about 80 m. The temperature difference between the northward and southward flowing branches of this shallow roll is ~2°C, so as noted in Wacogne and Pacanowski [1996] and Schott et al [2009], it does not on average significantly contribute to large scale hemispheric heat exchange.

3.2 Mean Seasonal Cycle

As shown in previous studies [*Hsiung,* 1985*; Schott et al.,* 2002*; Miyama et al.,* 2003*; Chirokova and Webster,* 2006], the meridional circulation in the Indian Ocean displays a dramatic seasonal reversal of cross equatorial flow in response to monsoon wind forcing. To illustrate these seasonal variations from our data, we compute the mean seasonal cycle of vertically integrated meridional flow over the upper 140 m using data from 2004-2013. Most of the variability in meridional velocity is confined to this depth range (Figure 5c), though results would be similar for lower limits of integration from 100 m to 200 m. From our analysis, we see that depth integrated flow in the upper 140 m is southward during boreal summer and northward during boreal winter (Figure 5b). The magnitude and direction of this flow is in remarkable agreement with the wind stress curl and in anti-phase with local merdional winds (Figure 5a). The competition between the local meridional wind forcing and the wind stress curl forcing produces the equatorial roll, in which wind driven northward currents in the upper 40-50 m are often directed opposite to deeper flows that are responding curl forcing (Figure 5c). This equatorial roll structure is particularly noticeable from July to October.

This wind-forced seasonal meridional circulation is a stable feature of the general circulation as indicated by both the wind forcing and the meridional transport computed over differing periods. For example, the mean seasonal cycle of wind stress curl forcing at this location computed over the 9-year period November 2004 to October 2013 is essentially identical to that computed over the much longer 34-year period January 1979 to December 2013 (Figure 5a). Likewise, the mean seasonal cycle of depth integrated meridonal velocity computed over the shorter 5-period August 2008 to July 2013 (for which we have velocity data at neighboring latitudes) is essentially identical to that for the 9-year period November 2004 to October 2013, though the uncertainties are somewhat larger for the shorter record

(Figure 5b).

The wind stress curl is largely determined by the meridional structure of the zonal winds (Figure 6a). In particular, during boreal summer months, southwest monsoon winds are westerly north of the equator and easterly south of the equator, while the opposite holds true during the northeast monsoon of boreal winter. *Miyama et al.* [2003] and *Schott et al*. [2004, 2009] idealized this wind structure in terms of purely anti-symmetric mean seasonal zonal wind stress forcing varying linearly with latitude. For this idealized forcing, Ekman pumping (defined as $w_{EK}=\rho^{-1}\mathrm{curl}\ (\boldsymbol{\tau}/f)$) is zero, the flow is horizontally non-divergent and theoretically the meridional Sverdurp volume transport ($V_{Sv}=-\tau^{x}{}_{y}/\rho\beta$) is equal to the meridional Ekman transport ($V_{Ek}=-\tau^{x}/\rho f$) where τ^{x} is the zonal component of wind stress. In this idealization, the ocean adjusts on the time scale of an inertial period without generating equatorial waves, zonal pressure gradients or geostrophic flows. The oceanic response thus represents a succession of steady states on monthly time scales, valid for a range of latitudes spanning and including the equator. The purely anti-symmetric wind stress field along 80.5°E, superimposed on the Sverdrup transport calculated from the observed wind stress [$V=(\rho\beta)^{-1}\mathrm{Curl}\ \boldsymbol{\tau}$] illustrates this idealized relationship (Figure 6b; see also *Horii et al.,* [2013]).

We note however that the observed meridional volume transport is not identical to the Sverdrup transport and that the differences exhibit a coherent relationship with the equatorially symmetric component of the zonal winds (Figure 6c). The differences are smallest on the equator (right panel of Figure 6c), but flow at higher latitudes tends to be poleward in both hemispheres, with northward flow to the north and southward flow to the south of the equator. This meridionally divergent flow tends to be most pronounced when the symmetric component of the zonal winds is strongest, namely in boreal spring (May-June) and fall (November-December). These periods correspond, with lag of ≤ 1 month, to the monsoon transitions when strong westerly winds prevail along the equator.

It is known that the ocean adjusts to this zonal wind forcing via equatorial wave radiation that sets up zonal pressure gradients to balance the winds on time scales of a few weeks [*Yuan and Han,* 2006*; Nagura and McPhaden,* 2008*; Nagura and McPhaden,* 2010a]. Thus, on monthly time scales we should expect that the observed divergent meridional flow off the equator to be approximately in balance with the zonal pressure gradients set up by the westerly monsoon transition winds. This balance is evident in two different representations of the zonal geostrophic flow calculated at 2°N and 2°S (Figure 7). One is computed from the depth integrated zonal pressure gradient (P) in the upper 140 m based on the mean dynamic height field ($V^{(1)}_{geos}$=-$(\rho f)^{-1}P_x$) and the other is based on the difference between the total observed depth averaged meridional velocity in the upper 140 m minus the wind driven Ekman transport inferred from Tropflux wind stresses ($V^{(2)}_{geos}=V_{obs}-V_{Ek}$). These two quantities are in principle not exactly the same because $V^{(2)}$ includes time dependence, nonlinearly and other processes that are not included in the geostrophic balance. However, as discussed in *Nagura and McPhaden* [2008], these processes are of secondary importance in the depth integrated momentum balance on seasonal time scales in the equatorial Indian Ocean relative to zonal wind stress forcing and pressure gradient force. Thus, to within the uncertainties of the calculations, $V^{(1)}$ and $V^{(2)}$ are essentially identical at both 2°N and at 2°S. Moreover, the geostrophic flow at 2°N is roughly equal to and opposite of that at 2°S and approximately in phase with the zonal wind stress averaged over 2°N-2°S as would be expected based on the zonal pressure gradient set up by these winds. We expect these results based on data from 2008-2013 are representative of longer periods given the similarity in the zonal wind stress forcing for this the 5-year period vs that over a longer 9-year interval from 2004 to 2013 (Figure 7a).

In contrast to the divergent geostrophic flow in the thermocline, Ekman transport computed from the wind stress at 2°N and 2°S is on average convergent (Figure 7c), with flow generally to the south at 2°N and to the north at 2°S. This convergent circulation results from the zonal component of winds, which is in the mean westerly at these latitudes. Ekman transports in both hemispheres exhibit predominantly annual variations such that, relative to the mean, flow is more towards the south in boreal summer and more towards the north in boreal winter. These variations in Ekman transport at 2°N and 2°S resemble those for the Sverdrup transport both in magnitude and phasing (cf. Figures 5b and 6b) but it is clear that the two are not equivalent like simple idealizations of the meridional flow field would suggest [*Miyama et al*., 2013; *Schott et al*., 2004, 2009]. It is also interesting that when taking the difference of the Ekman transports at 2°N and 2°S, in-phase annual variations tend to cancel, emphasizing the semi-annual convergent flow associated with the semi-annual zonal wind stress forcing along the equator. Thus, to fully understand the near equatorial meridional circulation in the Indian Ocean, one must take into account zonal wind stress forcing and the associated pressure gradients variations.

4. Discussion

The annual mean and seasonal cycle of meridional currents presented in Figure 4-7 reveal features peculiar to the central equatorial Indian Ocean. In the equatorial Pacific and Atlantic, easterly trade winds drive shallow subtropical cells (STCs) in each hemisphere that are associated with near equatorial surface poleward Ekman flows and a subsurface equatorward geostrophic flows [*Johnson et al*., 2001; *Schott et al*., 2004]. In contrast, we find that flow is directed towards the equator in the surface layer and away from the equator in the thermocline of the equatorial Indian Ocean. The reason for this contrast between the ocean basins is that the zonal winds are on average westerly along the equator in the Indian Ocean and easterly in the Pacific and Atlantic. As a consequence, we expect mean downwelling to prevail along the equator in the Indian Ocean as opposed to upwelling as found in the Pacific and Atlantic. This downwelling favorable meridional circulation explains why on average no equatorial cold tongue develops in sea surface temperature in the Indian Ocean in contrast to the Pacific and Atlantic.

We also find that on average there is a southward transport across the equator in the upper 140 m driven by the wind stress curl. Mean southward cross-equatorial flow was detected from measurements made at 73°E in the mid-1970s [*McPhaden, 1982*] and 90°E from ADCP measurements made between 2000 and 2009 [*Horii et al., 2013*]. This flow represents the surface branch of the cross-equatorial cell that carries water upwelled off the equator in the Northern Hemisphere (e.g., along the coasts of Somalia, the Arabian Peninsula, and Sri Lanka) back towards subduction zones in the Southern Hemisphere subtropics. This hemispherically asymmetric cross-equatorial cell is in sharp contrast to the more hemispherically symmetric STCs in the Pacific and Atlantic. Moreover, because of the competing effects of the wind stress curl favoring mean southward flow and the meridional wind stress favoring northward flow at the equator, a shallow equatorial roll develops, which is a unique feature of the Indian Ocean circulation.

Mean seasonal variations are also strikingly different between the Indian Ocean and the other two ocean basins. In the Pacific and Atlantic the zonal and meridional circulation waxes and wanes with season depending on the strength of the trades [e.g., *Philander and Pacanowski*, 1986; *Richardson and Walsh*, 1986; *Yu and McPhaden*, 1999; *Johnson et al*., 2002]. In contrast, dramatic cross-equatorial flow reversals occur in the Indian Ocean in response to monsoon wind forcing. Flow is generally from the summer to the winter hemisphere, transporting heat across the equator to moderate seasonal climate variability in the region [*Hsiung,* 1985*; Hsiung et al.,* 1987*; Wacongne and Pacanowski,* 1996]. In addition to these predominantly annual period cross equatorial flows, strong zonal winds associated with the monsoon transitions generate the semi-annual period Wyrtki jets [*Wyrtki*, 1973], intense eastward flowing zonal currents that have no analog in the Pacific and Atlantic. These jets are fed in part by convergent Ekman flow in the surface layer. They also transport significant mass from west to east [*McPhaden et al*., 2015], setting up a transient zonal pressure gradient force in the upper ocean. This pressure gradient force, which is directed to the west, lags the winds by a few weeks due to equatorial wave adjustment [*Yuan and Han*, 2006; *Nagura and McPhaden*, 2008; *Nagura and McPhaden*, 2010a] and amplifies divergent geostrophic flow in the thermocline relative to the annual mean.

5. Summary

In this paper we have examined circulation patterns in the central equatorial Indian Ocean using nine years of moored ADCP time series data between 2004 and 2013 in conjunction with Argo profile data and Tropflux wind stress data. Key findings are that the mean depth integrated volume transport is southwards across the equator in Sverdrup balance with the wind stress curl. Embedded in this southward transport is a shallow northward wind-driven frictional mean flow, which leads to an equatorial roll in the surface layer. The temperature difference between the northward and southward flowing branches of the roll is ~2°C, so as noted in previous studies it does not on average significantly contribute to cross equatorial heat transport. Mean westerly winds near the equator drive Ekman convergence in the surface layer and geostrophic divergence in the thermocline, implying a downwelling circulation that is in sharp contrast to the mean equatorial upwelling circulation that occurs in the equatorial Pacific and Atlantic Oceans in response to easterly trade wind forcing. The center of surface convergence and thermocline divergence is shifted downwind off the equator to about 0.75°N because of the mean northward wind stress component in the central equatorial Indian Ocean.

The mean seasonal cycle is characterized by pronounced annually reversing cross-equatorial volume transport variations in approximate steady state balance with annual variations in wind stress curl. Frictional counterflow develops at the surface from July in response to northward wind stress forcing during the southwest monsoon at a time when significant negative curl drives southward volume transport. These competing forces lead to the generation of a transient equatorial roll that persists into boreal fall. Superimposed on the annual cycle are significant semi-annual variations in Ekman convergence in the surface layer and geostrophic divergence in the thermocline forced by semi-annual variations in westerly wind stress. These westerly wind stresses are strongest during the monsoon transition seasons of April-May and October-November, leading to the set of up zonal pressure gradients along the equator in geostrophic balance with poleward thermocline flows in both hemispheres.

Our documentation of meridional circulation patterns in the central equatorial Indian Ocean is the most comprehensive to date based on direct velocity measurements. From these observations we are able to confirm some basic expectations from wind-driven theories of ocean circulation, demonstrating both the uniqueness and complexity of the mean seasonally varying meridional currents in this region. There are, however, still questions that require further research. For instance, the peak divergent geostrophic flow in May-June is significantly larger than the peak flow in October-December (Figure 6a) while westerly wind forcing and the Wyrtki jets tend to be stronger in the boreal fall rather than boreal spring for the time period covered by our data [*McPhaden et al*., 2015]. This disparity may be related to the wave dynamics associated with the zonal wind stress forcing, but it requires further investigation. Also, the structure of the meridional velocity field indicates equatorial downwelling is prevalent in the central basin, but its magnitude and seasonal evolution require additional analysis. How the meridional circulation varies zonally and from year-to-year along the equator likewise requires further study [see for example, *Horii et al*., 2013 for a preliminary discussion of these issues]. Our analysis provides a starting point for considering these and other outstanding issues. Moreover, despite the fact that many questions remain unanswered about the meridonal circulation in the equatorial Indian Ocean, we expect that our results will be valuable for validating circulation models models used for climate research and forecasting.

Acknowledgments

Special thanks to the Ministry of Earth Sciences (MoES) of India for providing the ship time necessary to maintain RAMA and the ADCP array; and to NOAA for providing RAMA and ADCP mooring equipment. Argo data can be obtained from the University of Hawaii at http://apdrc.soest.hawaii.edu/projects/Argo/data/Documentation/gridded-var.pdf and Tropflux wind stresses from http://www.incois.gov.in/tropflux/. Moored time series data are available from PMEL. We thank Professor Liu Qinyu in OUC for helpful discussions and two anonymous reviewers for their constructive comments on an earlier version of this manuscript. Yi Wang is supported by Natural Science Foundation of China (NSFC) no. 41490643 and NSFC-Shandong Joint Fund for Marine Science Research Centers no. U1406401, and Michael J. McPhaden is supported by NOAA. This is PMEL contribution no. 4581.

References

Chirokova, G., and P. J. Webster (2006), Interannual variability of Indian Ocean heat transport. *J. Clim.,* 19(6), 1013-1031.

Cromwell, T. (1953), Circulation in a meridional plane in the central equatorial Pacific. *J. Mar. Res.,*, 12(2), 196-213.

De Szoeke, S. P., S. P. Xie, T. Miyama, K. J. Richards, and R. J. O.Small (2007), What Maintains the SST Front North of the Eastern Pacific Equatorial Cold Tongue?. *J. Clim.,* 20(11), 2500-2514.

Garternicht, U., and F. Schott (1997), Heat fluxes of the Indian Ocean from a global eddy‐resolving model. *J. Geophys. Res.,* 102(C9), 21147-21159.

Hastenrath, S., and L. Greischar (1991), The monsoonal current regimes of the tropical Indian Ocean: Observed surface flow fields and their geostrophic and wind-driven components. *J. Geophys. Res.,* 96(C7), 12619-12633

Horii, T., K. Mizuno, M. Nagura, T. Miyama, and K. Ando (2013), Seasonal and interannual variation in the cross‐equatorial meridional currents observed in the eastern Indian Ocean. *J. Geophys. Res.,* 118(12), 6658-6671.

Hsiung, J. (1985), Estimates of global oceanic meridional heat transport. *J. Phys. Oceanogr.,* 15(11), 1405-1413.

Hsiung, J., R. E. Newell, and T. Houghtby (1987), Annual variation of heat transport in the Pacific and Indian Oceans, *Nature*, 518-520

Jensen, T. G. (1993), Equatorial variability and resonance in a wind - driven Indian Ocean model. *J. Geophys. Res.,* 98(C12), 22533-22552.

Johnson, G. C., M. J. McPhaden, and E. Firing, (2001), Equatorial Pacific Ocean horizontal velocity, divergence, and upwelling. *J. Phys. Oceanogr.*, 31(3), 839-849.

Kumar, B. P., J. Vialard, M. Lengaigne, V. S. N. Murty, M. J. McPhaden, M. F. Cronin, and K. G. Reddy (2013), TropFlux wind stresses over the tropical oceans: evaluation and comparison with other products. *Clim. Dyn.,* 40(7-8), 2049-2071.

Lazar, A., T. Inui, P. Malanotte-Rizzoli, A. J. Busalacchi, L. Wang, and R. Murtugudde (2002), Seasonality of the ventilation of the tropical Atlantic thermocline in an ocean general circulation model. *J. Geophys. Res.,* 107, 3104, doi:10.1029/2000JC000667.

Lee, T., and J. Marotzke (1997), Inferring meridional mass and heat transports of the Indian Ocean by fitting a general circulation model to climatological data. *J. Geophys. Res.,* 102(C5), 10585-10602.

McCreary, J. P., P. K. Kundu, and R. L. Molinari (1993), A numerical investigation of dynamics, thermodynamics and mixed-layer processes in the Indian Ocean. *Prog. Oceanogr.,* 31(3), 181-244.

McPhaden, M. J. (1982). Variability in the central equatorial Indian Ocean. I. Ocean dynamics. *J. Mar. Res.,* 40, 157-176

McPhaden, M. J., G. Meyers, K. Ando, Y. Masumoto, V. S. N. Murty, M. Ravichandran, and W. Yu (2009), RAMA: The research moored array for African-Asian- Australian monsoon analysis and prediction. *Bull. Amer. Meteor.,* 90(4), 459.

McPhaden, M. J., Y. Wang, and M. Ravichandran (2015), Volume transports of the Wyrtki jets and their relationship to the Indian Ocean Dipole. *J. Geophys. Res.,* 120(8), 5302-5317.

Miyama, T., J. P. McCreary, T. G. Jensen, J. Loschnigg, S. Godfrey, and A. Ishida (2003), Structure and dynamics of the Indian-Ocean cross-equatorial cell. *Deep Sea Res., Part I,* 50(12), 2023-2047.

Nagura, M., and M. J. McPhaden (2008), The dynamics of zonal current variations in the central equatorial Indian Ocean. *Geophys. Res. Lett.,* 35(23).

Nagura, M., and M. J. McPhaden (2010a), Wyrtki jet dynamics: Seasonal variability. *J. Geophys. Res.,* 115(C7).

Nagura, M., and M. J. McPhaden (2010b), Dynamics of zonal current variations associated with the Indian Ocean dipole. *J. Geophys. Res.,* 115(C11).

Pérez-Hernández, M. D., A. Hernández-Guerra, T. M. Joyce, and P. Vélez-Belchí (2012), Wind-driven cross-equatorial flow in the Indian ocean. *J. Phys. Oceanogr.,* 42(12), 2234-2253.

Philander, S. G. H., & Pacanowski, R. C. (1986), A model of the seasonal cycle in the tropical Atlantic Ocean. *Journal of Geophysical Research: Oceans*, *91*, 14192-14206.

Rabe, B., F. A. Schott, and A. Köhl (2008), Mean circulation and variability of the tropical Atlantic during 1952–2001 in the GECCO assimilation fields. *J. Phys. Oceanogr.*, 38(1), 177-192.

Rao, R. R., T. Horii, Y. Masumoto, and K. Mizuno (2016), Observed variability in the upper layers at the Equator, 90° E in the Indian Ocean during 2001–2008, 2: meridional currents. *Clim. Dyn.,* 1-18.

Reppin, J., F. A. Schott, J. Fischer, and D. Quadfasel (1999), Equatorial currents and transports in the upper central Indian Ocean: Annual cycle and interannual variability. *J. Geophys. Res.,* 104(C7), 15495-15514.

Richardson, P. L. and D. Walsh (1986), Mapping climatological seasonal variations of surface currents in the tropical Atlantic using ship drifts. *Journal of Geophysical Research: Oceans*, *91*, 10537-10550

Schott, F. A., and J. P. McCreary (2001), The monsoon circulation of the Indian Ocean. *Prog. Oceanogr.,* 51(1), 1-123.

Schott, F. A., M. Dengler, and R. Schoenefeldt (2002), The shallow overturning circulation of the Indian Ocean. *Prog. Oceanogr.,* 53(1), 57-103.

Schott, F. A., J. P. McCreary, and G. C. Johnson (2004), Shallow overturning circulations of the tropical‐subtropical oceans. *Earth's Climate*, 261-304.

Schott, F. A., S. P. Xie, and J. P. McCreary (2009), Indian Ocean circulation and climate variability. *Rev. Geophys.,* 47(1).

Sengupta, D., R. Senan, V. S. N. Murty, and V. Fernando (2004), A biweekly mode in the equatorial Indian Ocean. *J. Geophys. Res.,* 109(C10).

Sprintall, J., and M. Tomczak (1992), Evidence of the barrier layer in the surface layer of the tropics. *J. Geophys. Res.,* 97(C5), 7305-7316.

Wacongne, S., and R. Pacanowski (1996), Seasonal heat transport in a primitive equations model of the tropical Indian Ocean. *J. Phys. Oceanogr.,* 26(12), 2666-2699.

Wang, Y., M. J. McPhaden, H. P. Freitag, and C. Fey (2015): Moored Acoustic Doppler Current Profiler Time Series in the Central Equatorial Indian Ocean. *NOAA/PMEL Tech. Memo* OAR-PMEL-146. National Oceanic and Atmospheric Administration, Washington DC, 23 pp.

Wyrtki, K. (1973), An equatorial jet in the Indian Ocean. *Science*, 181, 262-264.

Yuan, D., and W. Han (2006), Roles of equatorial waves and western boundary reflection in the seasonal circulation of the equatorial Indian Ocean. *J. Phys. Oceanogr.,* 36(5), 930-944.

Figure Captions

Figure 1: (a) and (b) Location of the ADCP mooring sites (green triangles) superimposed on of surface wind stress vectors and calculated meridional Sverdrup volume transports (color shading) for (a) February and (b) August climatological means based on Tropflux wind data for the period 2008 to 2013; (c) availability of moored ADCP velocity data (black) and current meter data at 10 m depth (red).

Figure 2: (a) Meridional velocity estimated via a quadratic spline extrapolated to 10 m depth from ADCP data compared to measured velocity at 10 m depth at 1.5°, 0°, and 1.5°S, 80.5°E. (b) Meridional velocity estimated via linear least squares orthogonal regression for the period May 2010 to July 2011 compared to observed velocities for the same period in three depth ranges. All the time series have been smoothed with a 5-day running mean filter. Crosscorrelation coefficients and Root Mean Square Differences (RMSD) for each ensemble are shown in the upper left quadrants.

Figure 3: Meridional currents (in m s^{-1}) observed at 0°, 80.5°E. Time series of daily averaged data in (a) are smoothed with a 5-day running mean. Screened segments of the time series indicate gaps that have been filled via either linear least squares orthogonal regression or quadratic spline extrapolation as described in the text. Record length means of the time series ± one standard error are shown in (b) where the dashed line denotes values based on the quadratic spline extrapolation.

Figure 4: (a) Mean zonal (τ^x) and meridional (τ^y) wind stress components and wind stress curl between 2.5°N and 4°S along 80.5°E. The curl is computed using central differences on a 1° latitude × 1° longitude grid. Shading indicates ± one standard error. (b) Mean

meridional currents are shown as vectors overplotted on ocean temperatures (color shading). Only velocity values larger than 0.01 m s^{-1} are shown. The dashed black contours denote the zonal pressure gradient force computed from absolute dynamic height data. The pink solid line is the isothermal layer depth defined as the depth at which temperatures are 0.5°C lower than at 10 m. The dashed pink line is the mixed layer depth based on the density equivalent of 0.5°C decrease from 10 m using the method of *Sprintall and Tomczak* [1992]. Green triangles indicate the locations of the mooring sites.

Figure 5: The mean seasonal cycle at 0°, 80.5°E of (a) meridional wind stress (τ^y) and meridional Sverdrup transports [$V_{Sv}=(\rho\beta)^{-1}$Curl τ], (b) vertical integral of observed meridional currents in the upper 140 m, and (c) meridional velocity as a function of depth in the upper 200 m. Daily data for all time series were first smoothed with a 61-day triangle filter before computing the seasonal cycle, then smoothed again with a 7-day running mean to reduce noise and end point effects evident in late October in panel (c) for example where the start (27 October 2004) and end (26 October 2013) of the 10 year records have different values. The Sverdrup transports in (a) are computed for two different time periods, namely November 2004 to October 2013 and January 1979 to December 2013. Vertical integrals in (b) are also computed for two different time periods, namely November 2004 to October 2013 and August 2008 to July 2013. Shading in (a) and (b) indicates ± one standard error.

Figure 6: The mean seasonal cycle of (a) measured meridional mass transports computed as the depth averaged velocity in the upper 140 m (color shading) and surface wind

stress (vectors), (b) Sverdrup transports (color shading) and the component of wind stress that is anti-symmetric about the equator (vectors), and (c) the differences between measured (a) and computed Sverdrup (b) transports (color shading) and the component of the wind stress that is symmetric about the equator (vectors). Right panels show the standard deviations of the transports shown in the left panels. Seasonal cycles are based on averages from 8 August 2008 to 7 August 2013. Daily data for all time series were first smoothed with a 61-day triangle filter before computing the seasonal cycle, then smoothed again with a 7-day running mean to reduce noise and end point effects. Wind stress vectors are plotted at monthly intervals only for clarity. Sverdrup transport is computed using centered differences on a 1° latitude × 1° longitude grid. The black solid line in (c) shows where the difference between the measured transport and computed Sverdrup transports equals one standard deviation of the meridional transport difference.

Figure 7: The mean seasonal cycle of (a) zonal wind stress averaged within 2°S-2°N, 75°E-85°E, (b) geostrophic meridional transport in the upper 140 m (lines), and the observed transport in the upper 140 m minus Ekman transport (bars) at 2°N (red) and 2°S (blue), (c) Ekman transport at 2°N (red), 2°S (blue), and the difference of 2°N minus 2°S (black). In (a), the red line is the average from August 2008 to July 2013 and the blue line is the average from November 2004 to October 2013. In (b), the observed velocity at 2°N and 2°S is obtained by interpolating between the velocities at mooring sites to the north and south, namely at 2.5°N and 1.5°N for the 2°N value and at 1.5°S and 2.5°S for the 2°S value. Shading in (a) (b) (c) and error bars in (b)

indicate ± one standard error.

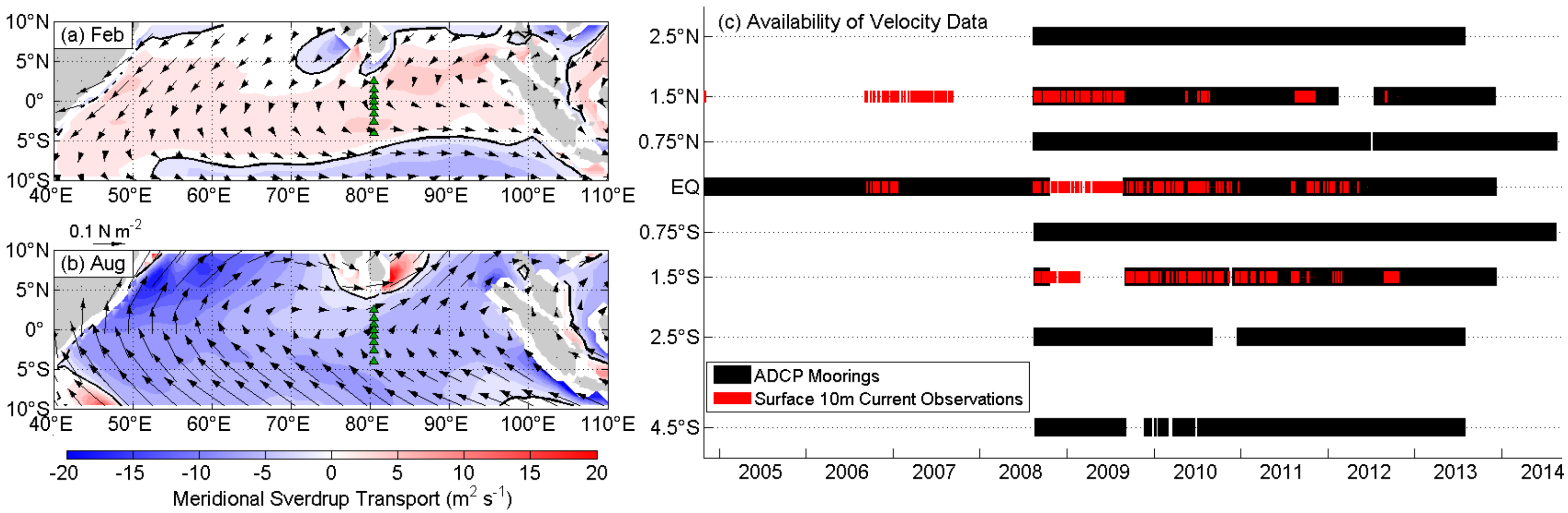

Figure 1: Location of ADCP mooring sites (green triangles) superimposed on surface wind stress vectors and calculated meridional Sverdrup volume transports (color shading) for (a) February and (b) August climatological means based on Tropflux wind data for the period 2008 to 2013; (c) availability of moored ADCP velocity data (black) and current meter data at 10 m depth (red).

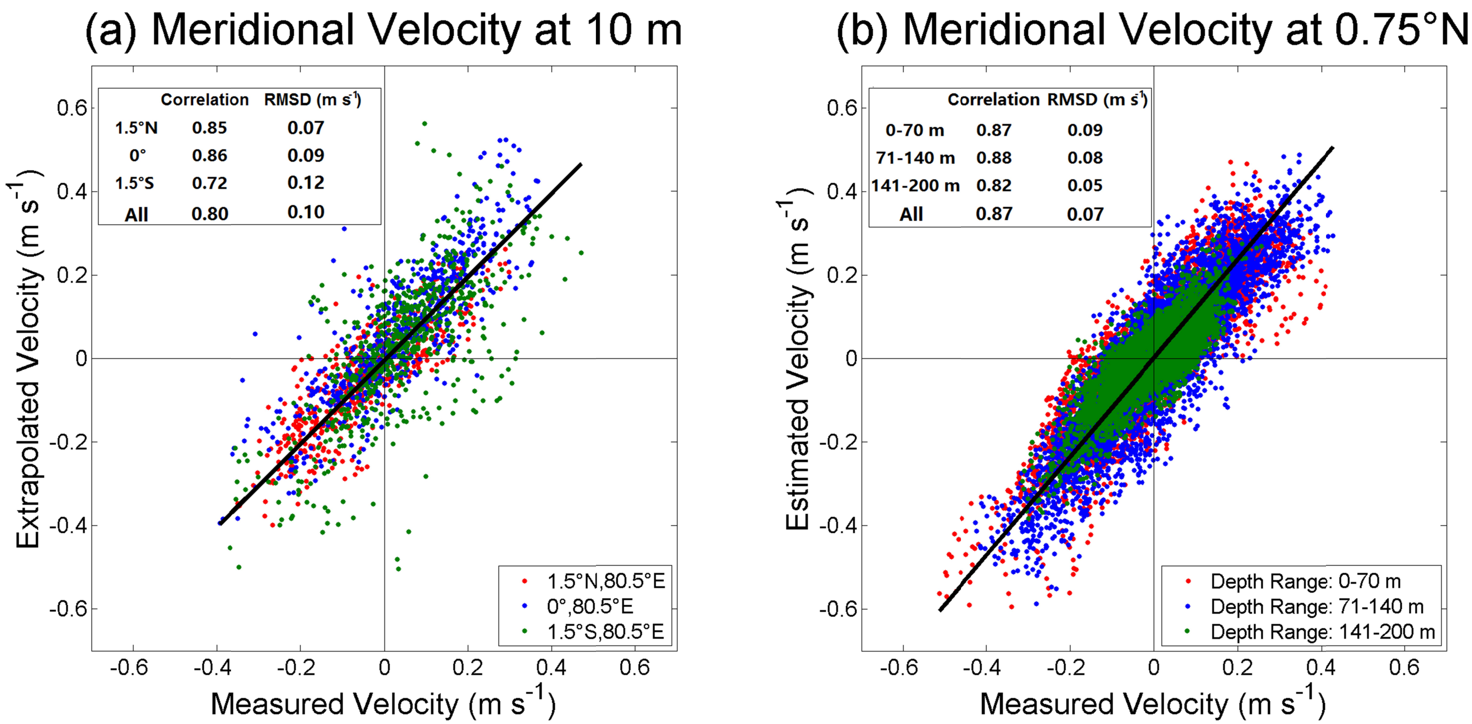

Figure 2: (a) Meridional velocity estimated via a quadratic spline extrapolated to 10 m depth from ADCP data compared to measured velocity at 10 m depth at 1.5°, 0°, and 1.5°S, 80.5°E. (b) Meridional velocity estimated via linear least squares orthogonal regression for the period May 2010 to July 2011 compared to observed velocities for the same period in three depth ranges. All the time series have been smoothed with a

5-day running mean filter. Cross-correlation coefficients and Root Mean Square Differences (RMSD) for each ensemble are shown in the upper left quadrants.

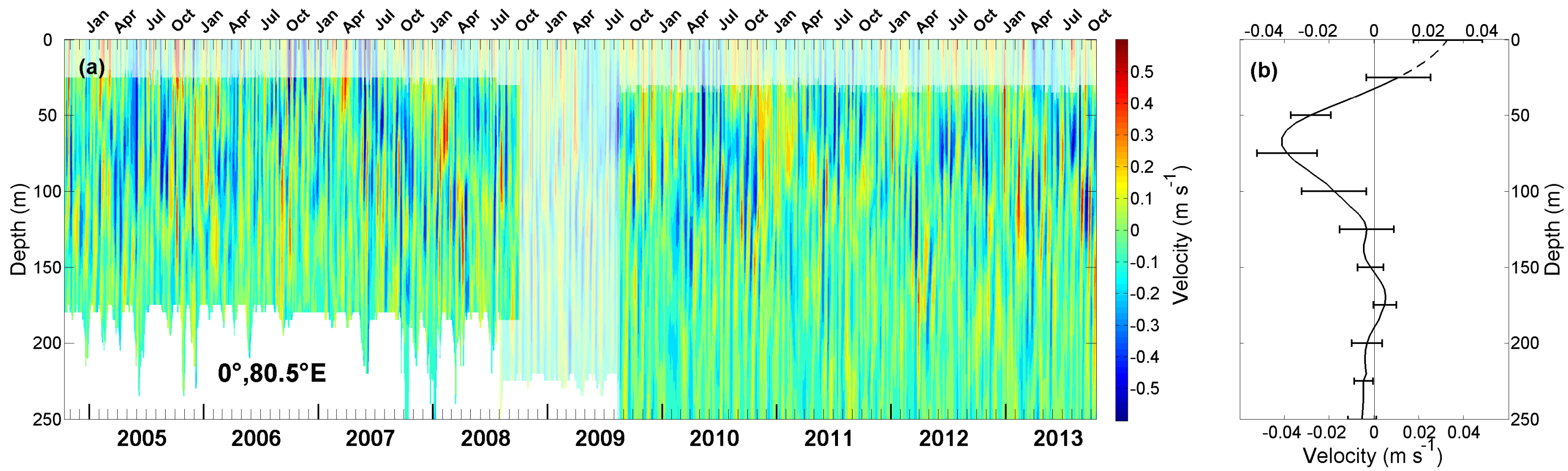

Figure 3: Meridional currents (in m s^{-1}) observed at 0°, 80.5°E. Time series of daily averaged data in (a) are smoothed with a 5-day running mean. Screened segments of the time series indicate gaps that have been filled via either linear least squares orthogonal regression or quadratic spline extrapolation as described in the text. Record length means of the time series ± one standard error are shown in (b) where the dashed line denotes values based on the quadratic spline extrapolation.

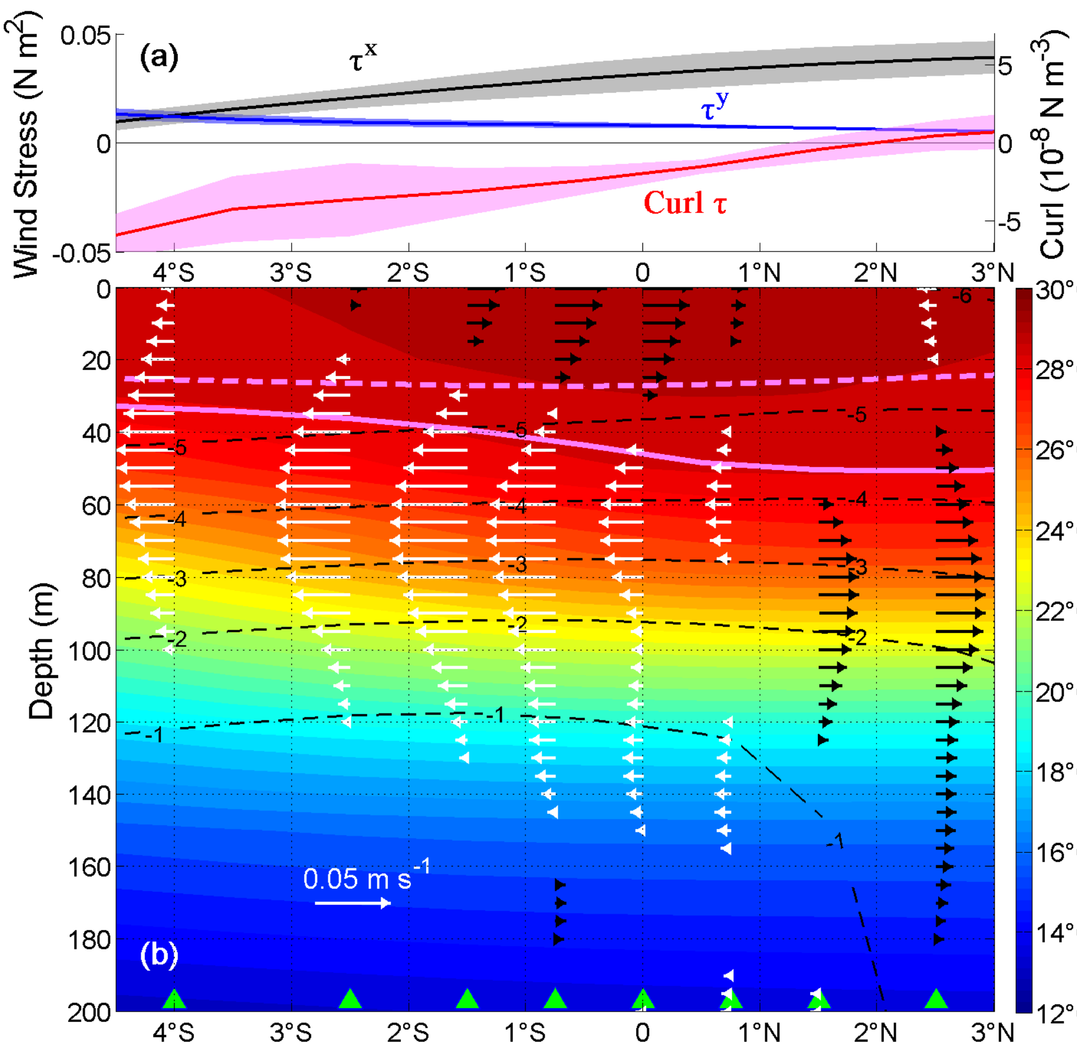

Figure 4: (a) Mean zonal (τ^x) and meridional (τ^y) wind stress components and wind stress curl between 2.5°N and 4°S along 80.5°E. The curl is computed using central differences on a 1° latitude × 1° longitude grid. Shading indicates ± one standard error. (b) Mean meridional currents are shown as vectors overplotted on ocean temperatures (color shading). Only velocity values larger than 0.01 m s^{-1} are shown. The dashed black contours denote the zonal pressure gradient force computed from absolute dynamic height data. The pink solid line is the isothermal layer depth defined as the depth at which temperatures are 0.5°C lower than at

10 m. The dashed pink line is the mixed layer depth based on the density equivalent of 0.5°C decrease from 10 m using the method of *Sprintall and Tomczak* [1992]. Green triangles indicate the locations of the mooring sites.

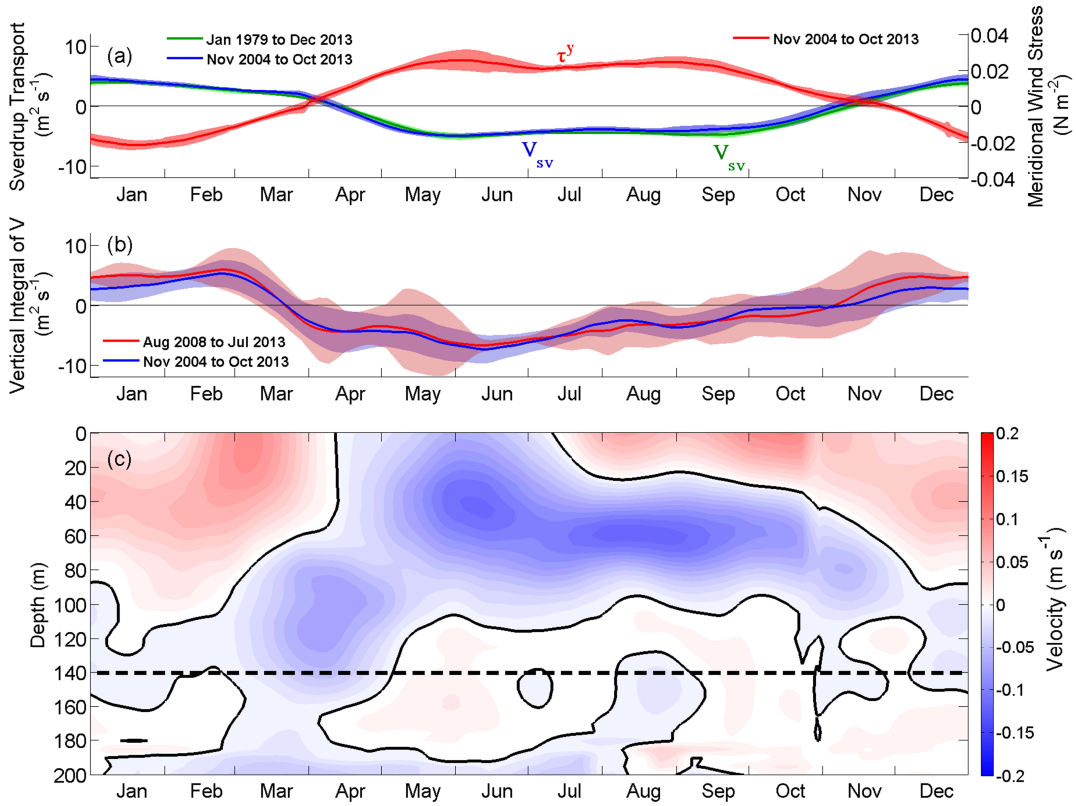

Figure 5: The mean seasonal cycle at 0°, 80.5°E of (a) meridional wind stress (τ^y) and meridional Sverdrup transports [$V_{Sv}=(\rho\beta)^{-1}\mathrm{Curl}\ \tau$], (b) vertical integral of observed meridional currents in the upper 140 m, and (c) meridional velocity as a function of depth in the upper 200 m. Daily data for all time series were first smoothed with a 61-day triangle filter before computing the seasonal cycle, then smoothed again with a 7-day running mean to reduce noise and end point effects evident in late October in panel (c) for example where the start (27 October 2004) and end (26 October 2013) of the 10 year records have different values. The Sverdrup transports in (a) are computed for two different time periods, namely November 2004 to October 2013 and January 1979 to December 2013. Vertical integrals in (b) are also computed for two different time periods, namely November 2004 to October 2013

and August 2008 to July 2013. Shading in (a) and (b) indicates ± one standard error.

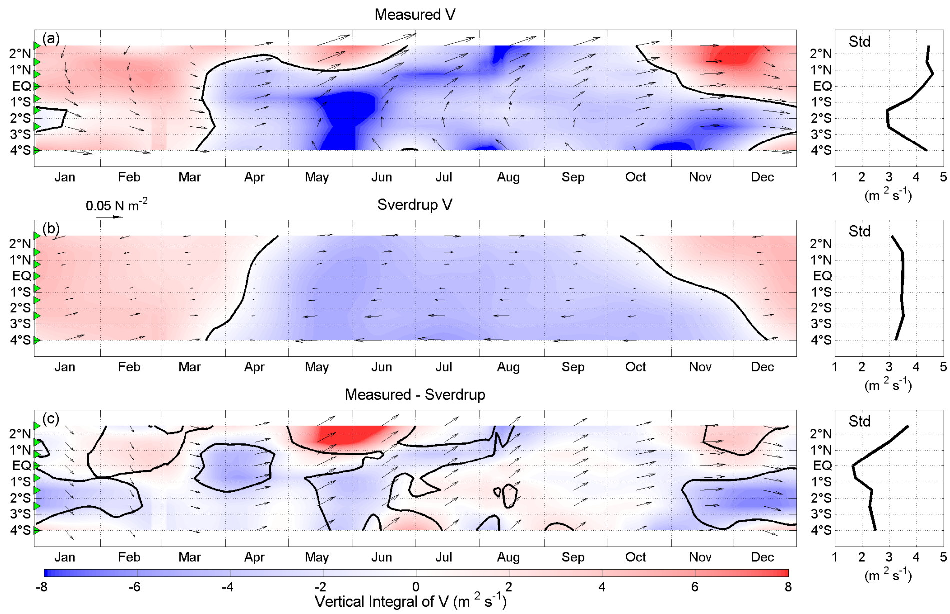

Figure 6: The mean seasonal cycle of (a) measured meridional mass transports computed as the depth averaged velocity in the upper 140 m (color shading) and surface wind stress (vectors), (b) Sverdrup transports (color shading) and the component of wind stress that is anti-symmetric about the equator (vectors), and (c) the differences between measured (a) and computed Sverdrup (b) transports (color shading) and the component of the wind stress that is symmetric about the equator (vectors). Right panels show the standard deviations of the transports shown in the left panels. Seasonal cycles are based on averages from 8 August 2008 to 7 August 2013. Daily data for all time series were first smoothed with a 61-day triangle filter before computing the seasonal cycle, then smoothed again with a 7-day running mean to reduce noise and end point effects. Wind stress vectors are plotted at monthly intervals only for clarity. Sverdrup transport is computed using centered differences on a 1° latitude × 1° longitude grid. The black solid line in (c) shows where the difference between the measured transport and computed Sverdrup transports equals one standard deviation of the meridional transport difference.

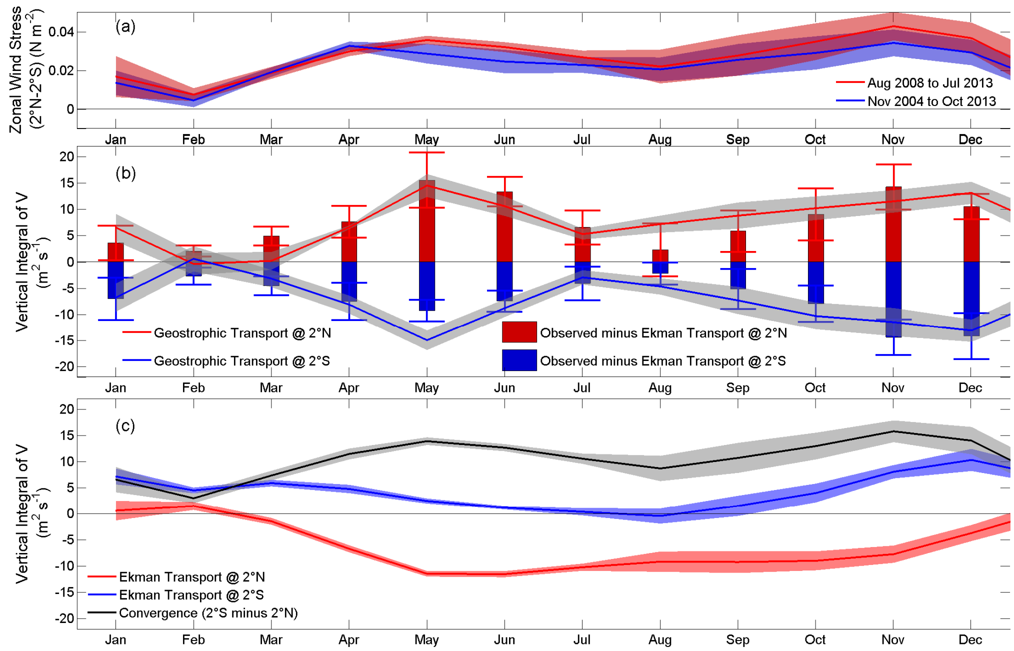

Figure 7: The mean seasonal cycle of (a) zonal wind stress averaged within 2°S-2°N, 75°E-85°E, (b) geostrophic meridional transport in the upper 140 m (lines), and the observed transport in the upper 140 m minus Ekman transport (bars) at 2°N (red) and 2°S (blue), (c) Ekman transport at 2°N (red), 2°S (blue) and the difference of 2°N minus 2°S (black). In (a), the red line is the average from August 2008 to July 2013 and the blue line is the average from November 2004 to October 2013. In (b), the observed velocity at 2°N and 2°S is obtained by interpolating between the velocities at mooring sites to the north and south, namely at 2.5°N and 1.5°N for the 2°N value and at 1.5°S and 2.5°S for the 2°S value. Shading in (a) and error bars in (b) indicates ± one standard error.

Figure 1.

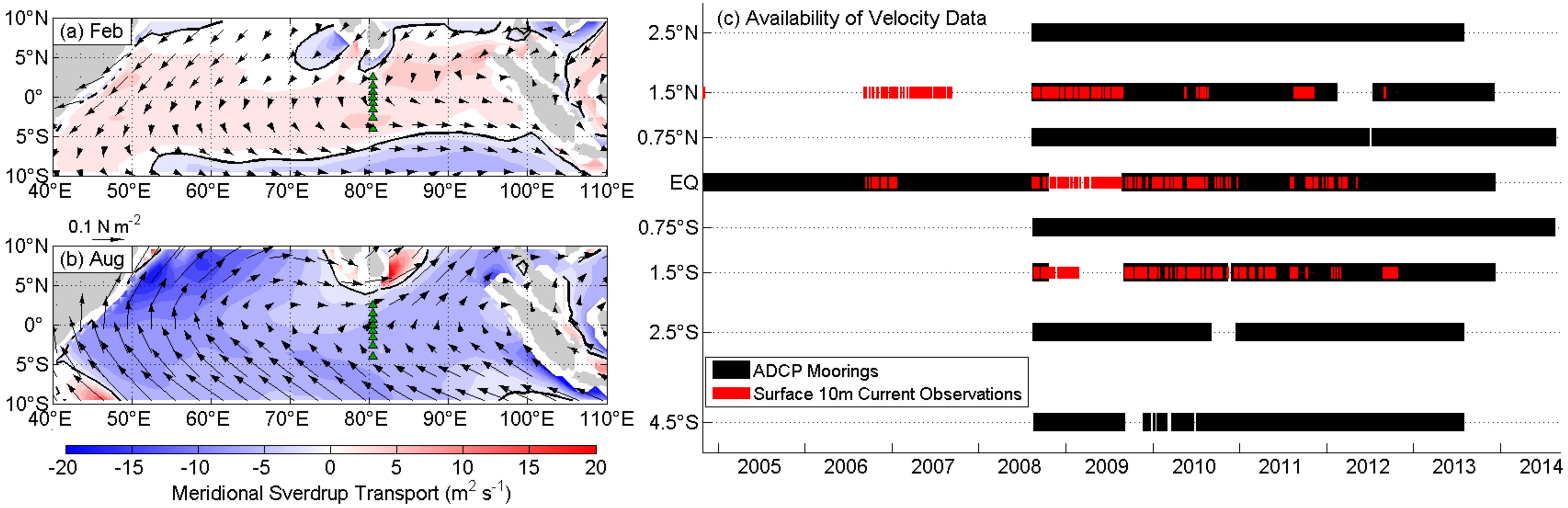

(a) Feb
(b) Aug
0.1 N m^{-2}
10°N
5°N
0°
5°S
10°S
40°E
50°E
60°E
70°E
80°E
90°E
100°E
110°E
-20
-15
-10
-5
0
5
10
15
20
Meridional Sverdrup Transport (m^2 s^{-1})
(c) Availability of Velocity Data
2.5°N
1.5°N
0.75°N
EQ
0.75°S
1.5°S
2.5°S
4.5°S
ADCP Moorings
Surface 10m Current Observations
2005
2006
2007
2008
2009
2010
2011
2012
2013
2014

Figure 2.

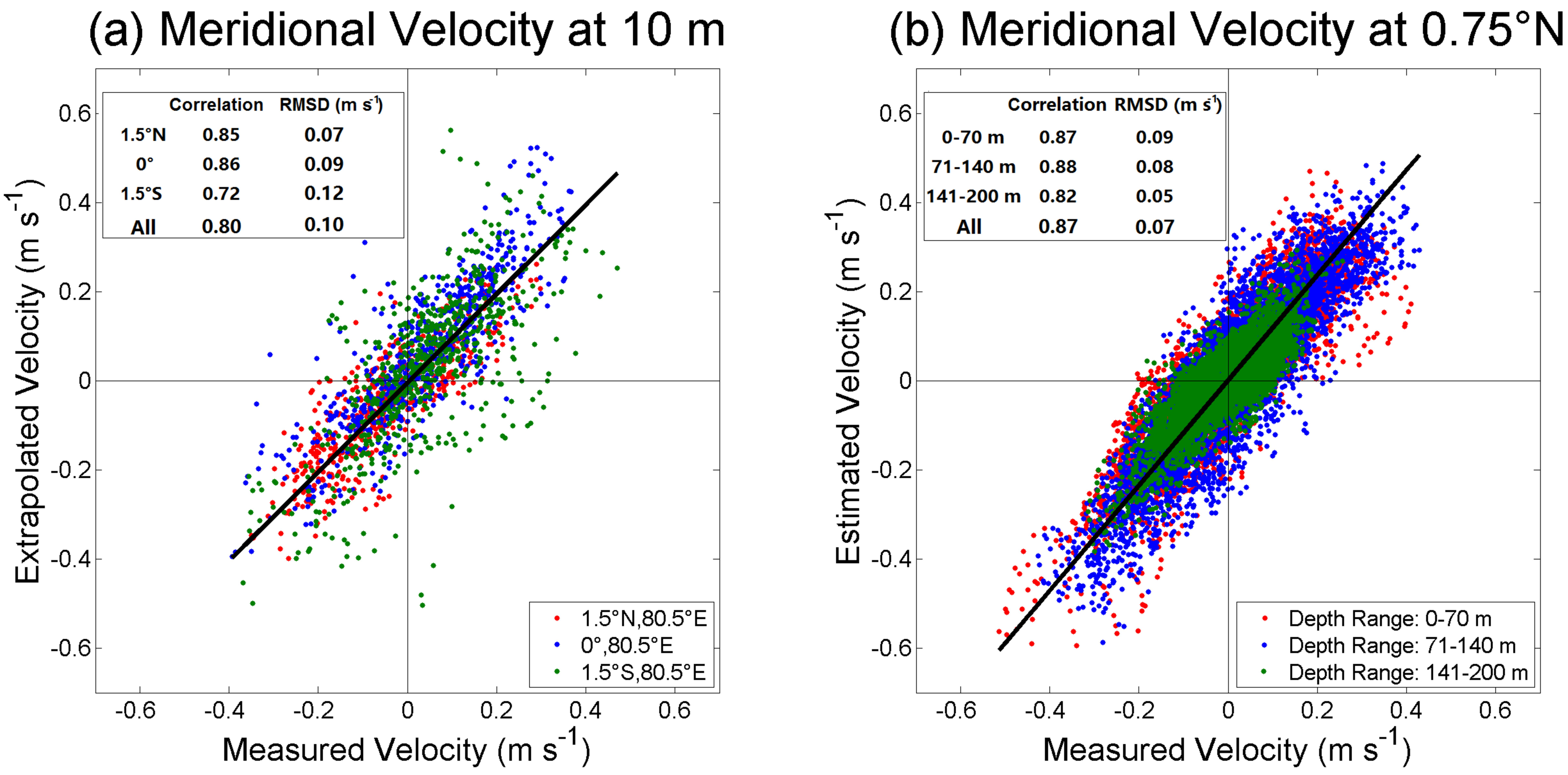

(a) Meridional Velocity at 10 m
Correlation RMSD (m s-1)
1.5°N 0.85 0.07
0° 0.86 0.09
1.5°S 0.72 0.12
All 0.80 0.10
Extrapolated Velocity (m s-1)
Measured Velocity (m s-1)
1.5°N,80.5°E
0°,80.5°E
1.5°S,80.5°E
(b) Meridional Velocity at 0.75°N
Correlation RMSD (m s-1)
0-70 m 0.87 0.09
71-140 m 0.88 0.08
141-200 m 0.82 0.05
All 0.87 0.07
Estimated Velocity (m s-1)
Measured Velocity (m s-1)
Depth Range: 0-70 m
Depth Range: 71-140 m
Depth Range: 141-200 m

Figure 3.

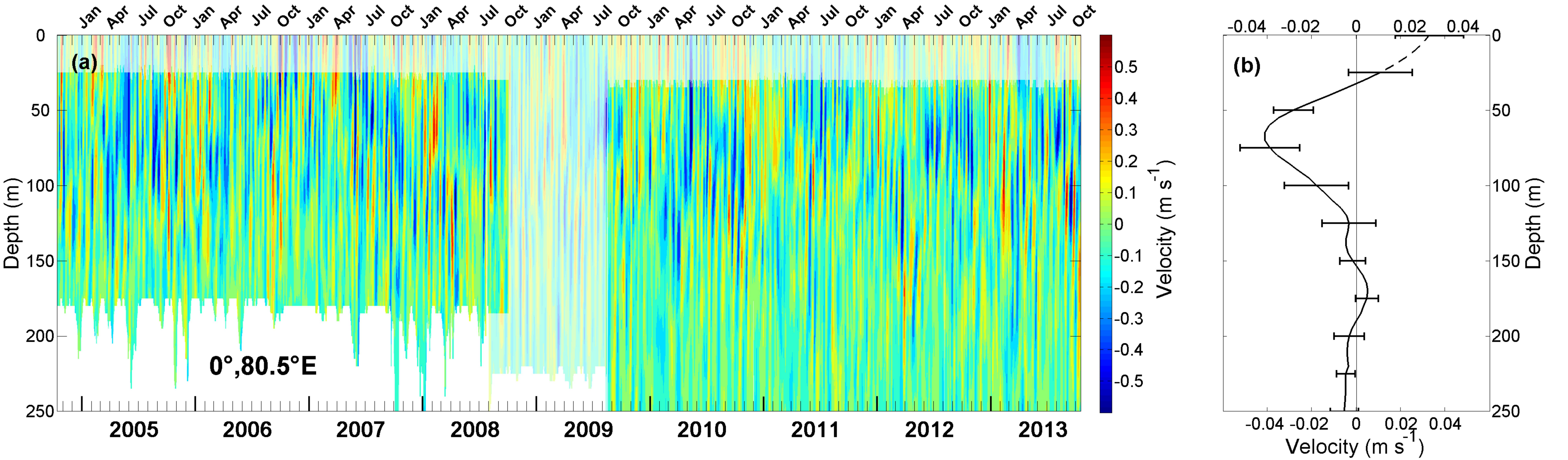

(a)
0°,80.5°E
Depth (m)
Velocity (m s-1)
2005
2006
2007
2008
2009
2010
2011
2012
2013
Jan
Apr
Jul
Oct
(b)
Velocity (m s-1)
Depth (m)

Figure 4.

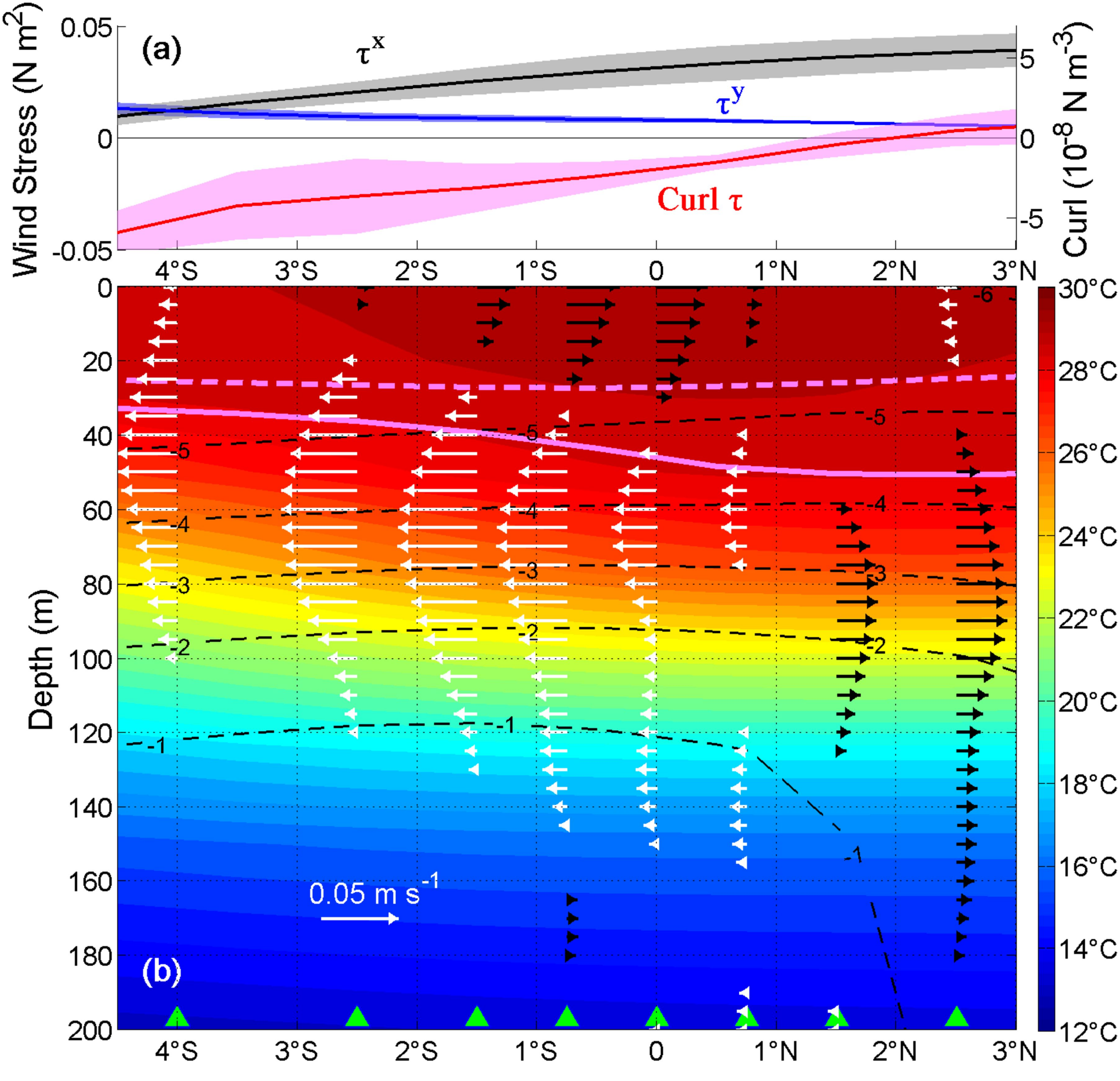

(a)
τ^x
τ^y
Curl τ
Wind Stress (N m^2)
Curl (10^{-8} N m^{-3})
0.05
0
-0.05
5
0
-5
4°S
3°S
2°S
1°S
0
1°N
2°N
3°N
Depth (m)
0.05 m s^{-1}
(b)
-6
-5
-4
-3
-2
-1
30°C
28°C
26°C
24°C
22°C
20°C
18°C
16°C
14°C
12°C

Figure 5.

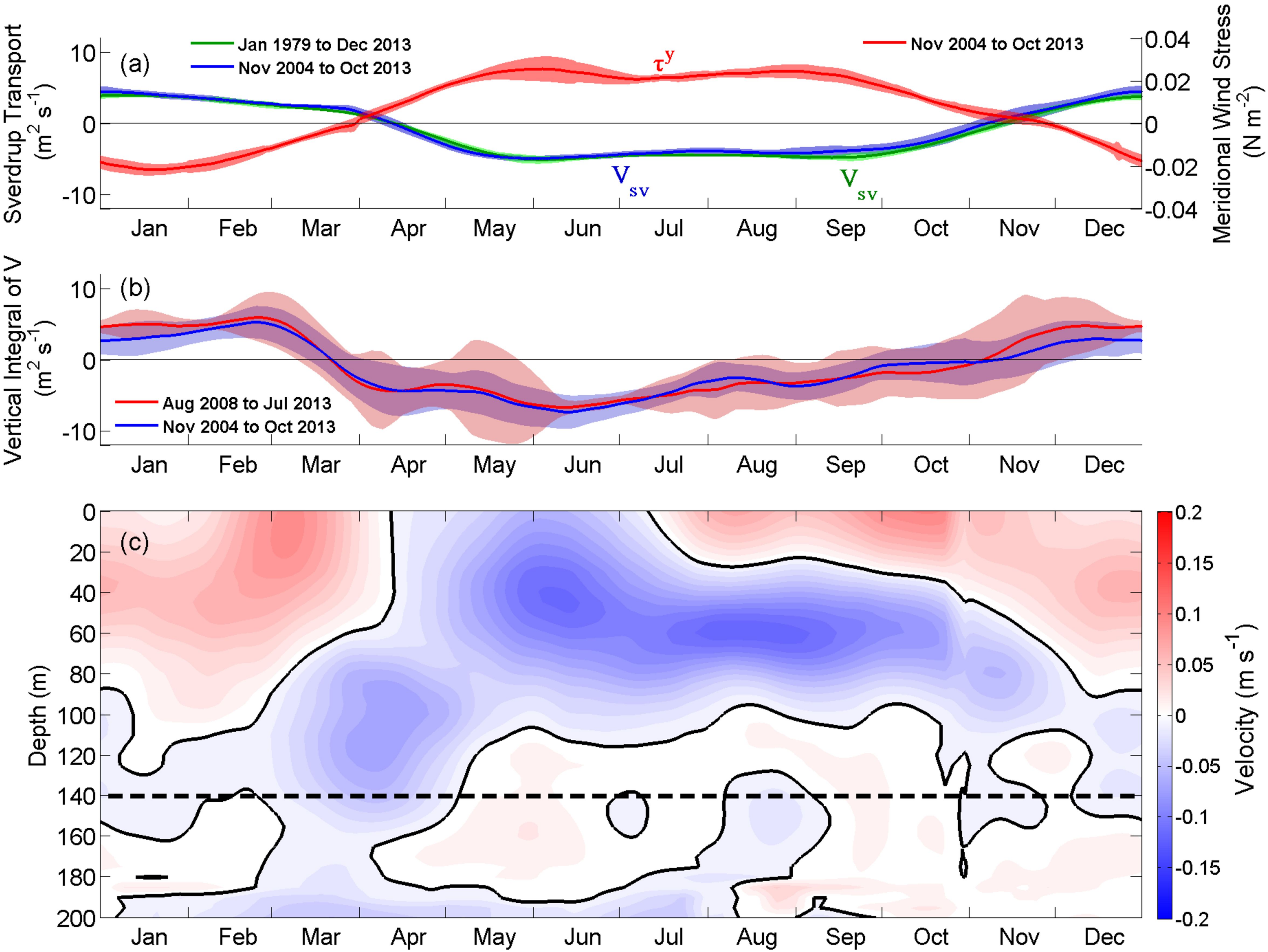

(a)
Jan 1979 to Dec 2013
Nov 2004 to Oct 2013
Nov 2004 to Oct 2013
τ^y
V_{sv}
V_{sv}
Sverdrup Transport ($m^2\ s^{-1}$)
Meridional Wind Stress ($N\ m^{-2}$)
(b)
Aug 2008 to Jul 2013
Nov 2004 to Oct 2013
Vertical Integral of V ($m^2\ s^{-1}$)
(c)
Depth (m)
Velocity ($m\ s^{-1}$)
Jan
Feb
Mar
Apr
May
Jun
Jul
Aug
Sep
Oct
Nov
Dec

Figure 6.

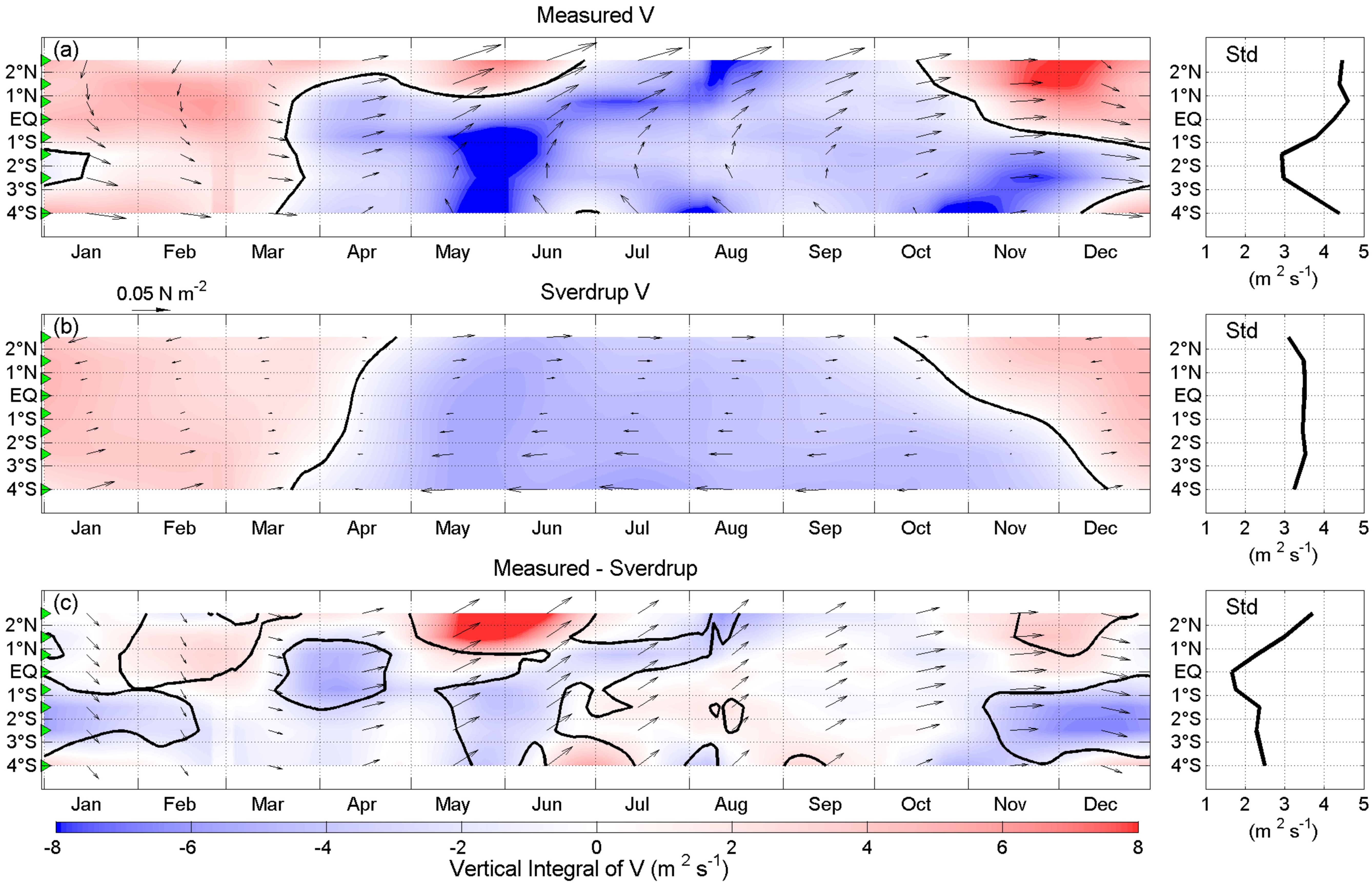
Measured V
(a)
Std
0.05 N m-2
Sverdrup V
(b)
Std
Measured - Sverdrup
(c)
Std
2°N
1°N
EQ
1°S
2°S
3°S
4°S
Jan
Feb
Mar
Apr
May
Jun
Jul
Aug
Sep
Oct
Nov
Dec
1
2
3
4
5
(m 2 s-1)
-8
-6
-4
-2
0
2
4
6
8
Vertical Integral of V (m 2 s-1)

Figure 7.

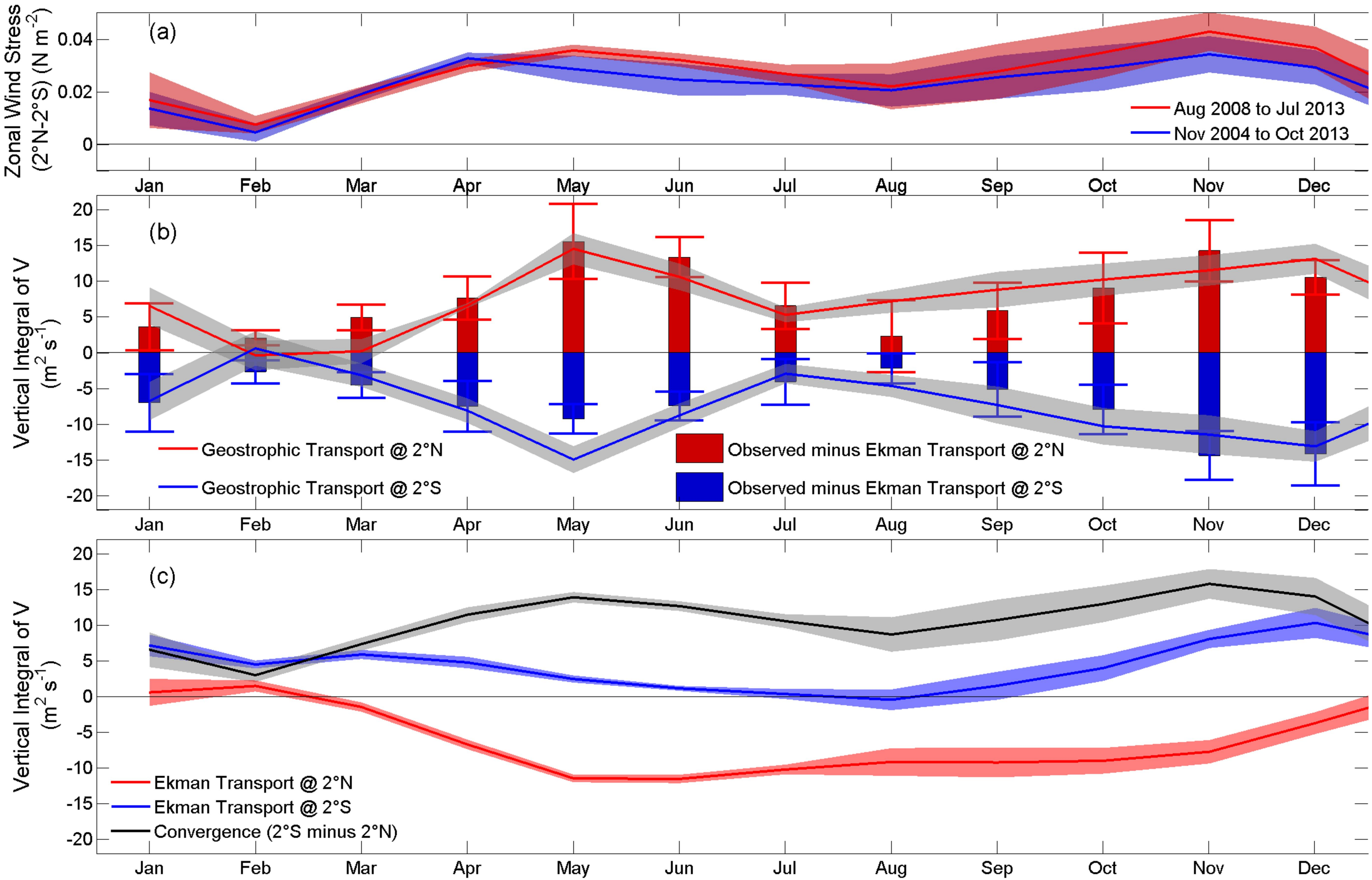
(a)
Zonal Wind Stress (2°N-2°S) (N m^{-2})
0.04
0.02
0
Aug 2008 to Jul 2013
Nov 2004 to Oct 2013
Jan
Feb
Mar
Apr
May
Jun
Jul
Aug
Sep
Oct
Nov
Dec
(b)
Vertical Integral of V (m^2 s^{-1})
20
15
10
5
0
-5
-10
-15
-20
Geostrophic Transport @ 2°N
Geostrophic Transport @ 2°S
Observed minus Ekman Transport @ 2°N
Observed minus Ekman Transport @ 2°S
Jan
Feb
Mar
Apr
May
Jun
Jul
Aug
Sep
Oct
Nov
Dec
(c)
Vertical Integral of V (m^2 s^{-1})
20
15
10
5
0
-5
-10
-15
-20
Ekman Transport @ 2°N
Ekman Transport @ 2°S
Convergence (2°S minus 2°N)
Jan
Feb
Mar
Apr
May
Jun
Jul
Aug
Sep
Oct
Nov
Dec